Tunable Anion-Selective Transport through Monolayer Graphene and Hexagonal Boron Nitride

Mustafa Caglar, Inese Silkina, Bertram T. Brown, Alice L. Thorneywork, Oliver J. Burton, Vitaliy Babenko, Stephen Matthew Gilbert, Alex Zettl, Stephan Hofmann, and Ulrich F. Keyser*

Cite This: https://dx.doi.org/10.1021/acsnano.9b08168

Read Online

ACCESS | Metrics & More | Article Recommendations | Supporting Information

ABSTRACT: Membranes that selectively filter for both anions and cations are central to technological applications from clean energy generation to desalination devices. 2D materials have immense potential as these ion-selective membranes due to their thinness, mechanical strength, and tunable surface chemistry; however, currently, only cation-selective membranes have been reported. Here we demonstrate the controllable cation and anion selectivity of both monolayer graphene and hexagonal boron nitride. In particular, we measure the ionic current through membranes grown by chemical vapor deposition containing well-known defects inherent to scalably produced and wet-transferred 2D materials. We observe a striking change from cation selectivity with monovalent ions to anion selectivity by controlling the concentration of multivalent ions and inducing charge inversion on the 2D membrane. Furthermore, we find good agreement between our experimental data and theoretical predictions from the Goldman−Hodgkin−Katz equation and use this model to extract selectivity ratios. These tunable selective membranes conduct up to 500 anions for each cation and thus show potential for osmotic power generation.

KEYWORDS: graphene, hBN, ion-selective membranes, GHK, charge inversion, anion-selective, tunable
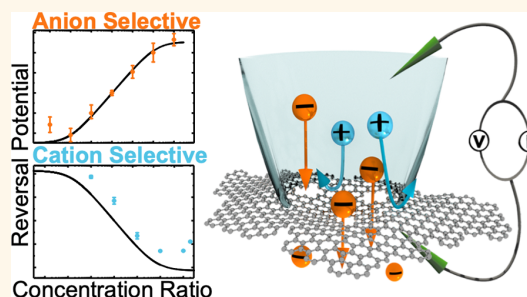
The pressing global need to improve technologies for generating clean energy and water desalination has triggered a flurry of research into porous ion-exchange membranes. Within these technologies, semipermeable membranes are used to separate two electrolytes and subsequently perform electrical, mechanical, or chemical work on the ionic flow. For example, ion-exchange membranes have been used as a component in electrodialysis and reverse osmosis (RO) processes[1] to desalinate and extract precious metal from wastewater. Both processes, however, are nonequilibrium because they require water to be driven through the membrane either electrically or by pressure, which is energy-intensive and thus limits their net output efficiency. Recent innovations in energy recovery systems have decreased the net energy consumption for pressure-driven RO by doing work with pressurized outputs;[2] however, developing more energetically efficient processes is key to the future of these technologies.[3]

Emergent technologies such as pressure-retarded osmosis and reverse electrodialysis minimize this problem even further by using a salinity gradient to drive ion flow, requiring no active fluid pumping. In both cases, a low resistance membrane is essential;[4] however, for reverse electrodialysis, a stack of both cation- and anion-selective membranes is required to generate power.[5] The performance of a membrane within these applications thus heavily depends on key metrics including the thickness of the membrane, the surface chemistry, and the pore distribution. 2D materials such as graphene and hexagonal boron nitride (hBN) can be tailored to meet many of these requirements, making them ideal candidates for use as ion-exchange membranes.[6] For example, their atomic thinness results in not only a decrease in resistance against fluid flux but also an intrinsic flexibility. In the case of graphene, the purely carbon composition makes surface functionalization relatively straightforward.[7] Control over surface properties is of particular interest because the selectivity of ion transport in 2D materials has been shown to arise predominantly due to extrinsic charging effects.[8−10] As such, changing the charge
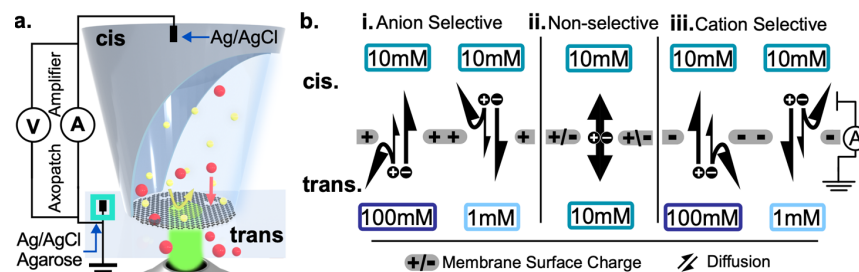
Figure 1. Experimental setup and ion-selectivity schematic for the transport of ions through a charged membrane driven by a salinity gradient alone. (a) Saline-solution-filled quartz capillary in contact with an Ag/AgCl electrode with a graphene membrane sealed onto the tip. The opposing side of the membrane is another Ag/AgCl electrode coated in an agarose salt bridge. Ion rejection (yellow arrow) and selective transport (red arrow) by a nanopore in the graphene membrane are shown (not drawn to scale). (b) Selective drift current is measured for imposed concentration gradients across membranes with different surface charges. The net drift current is shown in each case, with black arrows indicating the direction and magnitude of diffusive flow for: (i) an anion-selective membrane, (ii) a membrane between reservoirs of equal concentrations resulting in no net diffusive flux, and (iii) a cation-selective membrane.

polarity of the membrane potentially allows for manipulation of the magnitude and charge specificity of the membrane selectivity. This could provide a route to the anion-selective membranes required by power generation applications that are presently absent in the literature, in marked contrast with multiple previous demonstrations of cation selectivity.

A further challenge arises because, although some disagree with this notion,[11] it is almost universally accepted that the introduction of pores is critical to facilitating ionic transport. This is required because pristine graphene is impermeable to atoms as small as helium.[12] Whereas precisely fabricated pores are a popular choice for preparing porous membranes, the helium ion or electron beam processes used to create the pores come with significant overhead in cost, time, and yield.[13,14] Recently, however, selective transport has been demonstrated for chemical-vapor-deposited (CVD) membranes[8] which can be produced at scale and high throughput.[15−17] Transport here is due to defects inherent to current large-area CVD and linked wet-transfer processes,[18] removing the necessity for arduous pore-creation processes. Moreover, larger scale treatments for the controlled expansion of intrinsic defects are under development.[19−21] To fully exploit these materials, however, further efforts toward the characterization of the distribution of intrinsic defects and their contribution to selectivity is required, which is currently lacking.

Here we show anion-selective behavior in both monolayer CVD graphene and monolayer hBN suspended on aqueous media. We use CVD materials, which, except for a standard wet transfer, are not further processed. Therefore, we are not deliberately introducing defects but are assessing transport across typical defects alone. Our membranes are characterized using high-resolution transmission electron microscopy (HRTEM) and *in situ* Raman spectroscopy and by conductance measurements. We build a framework for studying ionic transport through defects by sealing 2D membranes onto quartz nanocapillaries[22] that are used to contact and manipulate the materials (Figure 1a). Electrical contact on both sides of the membrane allows current and voltage characteristics to be measured across the membrane from which selectivity can then be determined. We find that multivalent salts such as hafnium tetrachloride ($HfCl_4$) cause membranes to exhibit anion selectivity. This anion selectivity is most likely the effect of surface charge reversal[23−25] by the multivalent ion, with a change from negative to positive surface

charge causing a change from cation to anion selectivity. Moreover, anion selectivity of the membrane is also observed in monovalent salts—systems previously shown to exhibit cation-selective behavior—if a low background concentration of multivalent ions is added to the solution. We model membrane performance using Goldman−Hodgkin−Katz (GHK)[26] relations and provide a quantitative analysis of selectivity. There are stark differences in the chemical makeup and electrical characteristics between graphene and hBN; therefore, in studying transport across two monolayer materials, commonly observed phenomena indicate universality, supporting the isolation of their cause to extrinsic factors. Finally, to demonstrate the relevance of our system for technological applications, we calculate key metrics to assess the performance of these selective membranes as applied ion-exchange membranes.

RESULTS AND DISCUSSION

The method used to interface 2D membranes is described in the Experimental Methods and summarized in brief in Figure 1a. A quartz nanocapillary (nominal diameter ∼150 nm) is filled with saline solution and used to seal onto and pick up a piece of 2D material. The effect of the capillaries on ion selectivity is deemed negligible through a series of control experiments in the absence of a membrane.[8] *In situ* Raman spectroscopy (illustrated with a green laser) enables on-the-fly characterization of graphene. The capillary acts as a fixed cis reservoir that is then immersed into external trans reservoirs containing a variety of salts, exposing the sealed 2D material to distinct saline solutions. To establish membrane conductance and measure ionic transport, an amplifier is connected across the membrane using silver−silver/chloride electrodes. With this, voltages can be applied and the current can be monitored across the membrane and *vice versa*. The conductance of the capillary without the membrane is used to establish the size of the nanometer opening of the capillary, and the subsequent change in conductance upon contact with the 2D material gives an indication of the adherence of a 2D material on the capillary.

Transport across the 2D materials depends on the surface functionalization and charge, both termed extrinsic effects. Electrostatic charging of the surfaces of 2D materials on water has been demonstrated, with estimates for graphene on water[13] as −0.6 and −0.16 C/m^2 for hBN.[27] Such extrinsic charging on
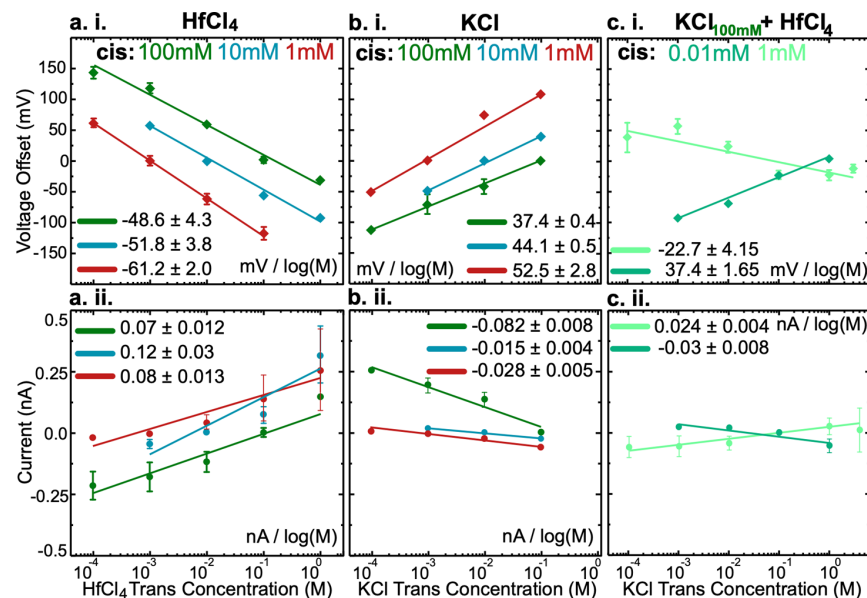
Figure 2. Tunable ion selectivity in different salt solutions. (a) HfCl$_4$ in cis and trans reservoirs. (i) Voltage offset as a function of the trans concentration for different cis concentrations, all indicating anion selectivity. The gradients of each line are given in the legend with the largest magnitude gradient for [cis] = 1 mM. The anion-selective current (ii) is similar across all cis concentrations. (b) Corresponding data for KCl showing in all cases the expected cation-selective behavior. (c) Voltage and current offsets for 100 mM KCl with a low background concentration of HfCl$_4$ showing a change in the selectivity from cation to anion with increasing concentration of HfCl$_4$.

both materials is most likely due to hydroxide adsorption,[28] and this surface charge will determine the behavior of the nanopore with respect to its electrostatic interactions with ions in solution. In Figure 1b, we illustrate the expected scenarios for ion flow through a charged semipermeable membrane separating two ionic solutions, analogous to the system in Figure 1a. Because diffusion drives ion flow down a salinity gradient, both cations and anions will tend to flow from a lower to a higher concentration. However, an imposed concentration gradient across the selective membrane results in the diffusive flow of predominately one type of ion. This net movement of either the cations or the anions in the system results in the observation of a current, with the current thus directly reflecting the selective behavior of the membrane. Note that here, for no driving voltage or current, measured voltages and currents are a result of the selective flux of ions down their concentration gradient alone.

The selective current will result in a reversal potential, V_{rev}, forming across the membrane, governed by the Nernst equation

$$V_{rev} = S \frac{RT}{zF} \ln\left(\frac{C_{trans}}{C_{cis}}\right) \tag{1}$$

where C_{trans} and C_{cis} are the concentrations in the trans/cis reservoirs respectively, R denotes the gas constant, T is the temperature, z is the ion valency, F is Faraday's constant, and S is the percentage of selectivity. The reversal potential indicates the potential that must be applied across the membrane to oppose the selective flux of ions arising from a concentration gradient. From eq 1, a system that is perfectly selective ($S = 1$) toward either the cation or anion in a monovalent species at 300 K would have an absolute reversal potential of 59.5 mV per decade molar concentration ratio (M) (mV/log(M)). Note that, a perfectly selective membrane toward anions will be

permeable for anions and impermeable toward cations. For most systems, the membrane will not be perfectly selective; that is, there will also be some flux of the counterion across the membrane that will reduce the measured current. Here the measurement of the reversal potential can be used to quantify how close the membrane reaches the perfectly selective case.

To explore this further, Figure 1b.i presents possible scenarios for transport across a charged membrane. A positive surface charge will result in a higher population of anions around the pore region, and thus transport through the pore is more preferential to anions, with only a fraction of cations also flowing (black arrows). The amount of cation flux across this otherwise anion-selective pore will depend on the pore's selectivity ratio. On the basis of this, a current measured with no applied driving potential would be positive when the cis concentration ([cis]) is less than the trans concentration ([trans]) and negative when [cis] > [trans]. The reversal potential, when the current is zero, should be negative for [cis] < [trans] and positive when [cis] > [trans]. Figure 1b.ii shows a pore with no salinity gradient across it, resulting in no net diffusive flow and rendering the pore nonselective. In measurements using our system, the case of equal cis and trans concentrations that should correspond to no measured current is used as a calibration point. Finally, Figure 1b.iii considers the case of a negatively charged surface, which results in cation-selective behavior. Applying similar logic, the negative surface charge will result in a higher population of cations around the pore, thus making their transport across the pore more likely. In this case, when [cis] < [trans], the current will be negative, and when [cis] > [trans], the current will be positive. Similarly, the reversal potential should be positive for [cis] < [trans] and negative when [cis] > [trans]. These scenarios thus outline how the drift current and the potential across the membrane resulting from the asymmetrical ion flow are direct quantifiers of selectivity.

Current−voltage (I−V) curves are measured for the system with different concentration gradients across the membrane. For each capillary, at least three I−V curves are recorded at each trans concentration, sampled at 10 mV steps, which are subsequently averaged, with error bars representing the spread in the data. (See the Experimental Methods.) An illustrated example of processing data from I−V curves to selectivity ratios is presented in the Supporting Information (SI), section S1. To assess the degree of the selectivity, we extract the current and voltage intercepts from I−V curves for a fixed cis concentration. These are then presented as a function of the trans concentration. The voltage intercepts are a direct measure of the built-up membrane potential, or the reversal potential, as expressed by eq 1. In line with this equation, we find a linear behavior of the reversal potential with changing the trans concentration on a log−linear scale. Inspection of eq 1 shows that the slope of this line should be directly related to the percentage selectivity, S. As such, gradients of the linear fits are used to provide a measure of the selectivity as the change in reversal potential with concentration (mV/log[M]). The gradient of the current−concentration plot (nA/log[M]) confirms the direction of the selectivity and provides an idea of the selective ionic flux across the pore(s). Here a negative gradient in the plot of the reversal voltage against [trans] corresponds to a positive selective current gradient (from the definition of conventional current) and thus indicates anion selectivity. The opposite behavior would be expected for cation-selective membranes. The direction of these gradients directly establishes which ions are diffusing across the membrane, whereas the magnitude of the gradient indicates the degree of this selectivity.

In Figure 2a, we explore the effect of a solution of HfCl$_4$ containing multivalent ions on the selectivity of monolayer graphene. Each line in the figure represented a different cis concentration for the same set of trans concentrations. Here the negative gradient in the plot of voltage offset versus concentration, or voltage selectivity (Figure 2a.i), shows that the membrane transport is dominated by chloride ions in all cases. We therefore find that anion-selective transport dominates in a system with HfCl$_4$. Furthermore, the magnitude of the slope, and thus the degree of anion selectivity, increases as the cis concentration decreases. From the extracted slopes and eq 1, the selectivity percentage, S, can be obtained. At 100 and 10 mM [cis], selectivity is at 82 and 88% of the theoretical maximum, respectively. Notably, selectivity reaches the theoretical maximum ($S = 1$) for a cis concentration of 1 mM. The current is further evidence of anion selectivity; however, here the magnitude appears to not significantly depend on the cis concentrations. Note that the same behavior is seen with another tetravalent ionic solution, zirconium tetrachloride (ZrCl$_4$), as shown in the SI, section S2. Moreover, hBN responds identically to that of graphene, as shown in the SI, section S3. All salt solutions used are unbuffered with measured conductivities and pH values that are presented in the SI, section S4.

For comparison, in Figure 2b, we show the equivalent behavior for cis and trans reservoirs filled with varying concentrations of KCl only. Here, as in previous reports,[7,9,13,29−32] transport is predominantly controlled by potassium ions, and, as such, plots of the voltage offset versus trans concentration all have a positive gradient. As with HfCl$_4$, the magnitude of the slope increases with decreasing cis concentration, although here the magnitudes are somewhat smaller than those for the multivalent case. In particular, we observe at 100 mM a selectivity of 64%, at 10 mM a selectivity of 75%, and the highest selectivity of 90% ($S = 0.9$) of the theoretical maximum for 1 mM in the cis reservoir. Our result is consistent with other observations[8] that note that selectivity is largely controlled by the highest ion concentration, as this alters the Debye screening length and thus the selectivity, which is yet another indication that the selectivity is due to extrinsic effects.

In light of the picture of selective transport outlined in Figure 1b, the contrasting behavior of the systems in Figure 2a,b suggests that whereas in the monovalent salt the membrane maintains a negative charge, with multivalent ions, the membrane instead develops a net positive charge. To further explore the effect of multivalent ions on positively charging the surface of the graphene, we now consider the effect on the selective transport in KCl of a small background concentration of HfCl$_4$. Figure 2c shows data from a system with 100 mM KCl in the cis reservoir and varying KCl concentrations in the trans reservoir with an addition of low concentrations of HfCl$_4$. With an addition of 0.01 mM HfCl$_4$, cation selectivity is observed, and at the same magnitude as seen without the addition of HfCl$_4$ (green data in Figure 2b). Interestingly, however, at an addition of 1 mM HfCl$_4$ to 100 mM KCl, a switch to anion selectivity is seen despite there being no gradient in HfCl$_4$ concentration across the system. Thus chloride ion filtration is shown with KCl by the use of a small but constant HfCl$_4$ background. The implication is that 1 mM HfCl$_4$ is sufficient to alter the graphene surface charge from negative to positive.[23,24] The mechanism by which this occurs is referred to as charge inversion[23,24] and, as an extrinsic process, is not a phenomena exclusive to 2D membranes. Furthermore, the reversibility of this inversion of surface charge implies that the process is purely electrostatic, as opposed to a surface chemical effect.

The crossover point from cation- to anion-selective behavior occurs between the addition of 0.1 and 1 mM of HfCl$_4$. Whereas the crossover concentration has previously not been determined for mixtures of monovalent and tetravalent ions, the crossover concentration in our experiments is consistent with that found for trivalent ions, where a crossover, or a point of charge inversion, has been observed at ∼0.2 mM.[24] Moreover, in repeating our experiment with trivalent salts, CeCl$_3$ and LaCl$_3$, we observe a point of charge inversion from cation to anion selectivity between 1 and 10 mM, with the decrease in value compared with that in the literature perhaps accounted for by differences between the inherent surface charge of the silica beads used in Dekker et al.[24] as opposed to the graphene surface used here; see the SI, section S5.

Considering the concentration ratio, that is, [cis]/[trans], across a range of fixed cis values gives a more holistic overall view of performance. Furthermore, this allows for a selectivity ratio to be extracted from GHK equations as a function of the concentration ratio and the ionic valency alone. This parameter provides a more ready comparison of selective flux for systems for which the direction and magnitude of selectivity differ. The GHK equation describes ionic flux across a membrane, as quantified by the transmembrane potential in terms of the ionic concentration ratio and the membrane selectivity ratio.[26] For the simplest case of a symmetric monovalent ion
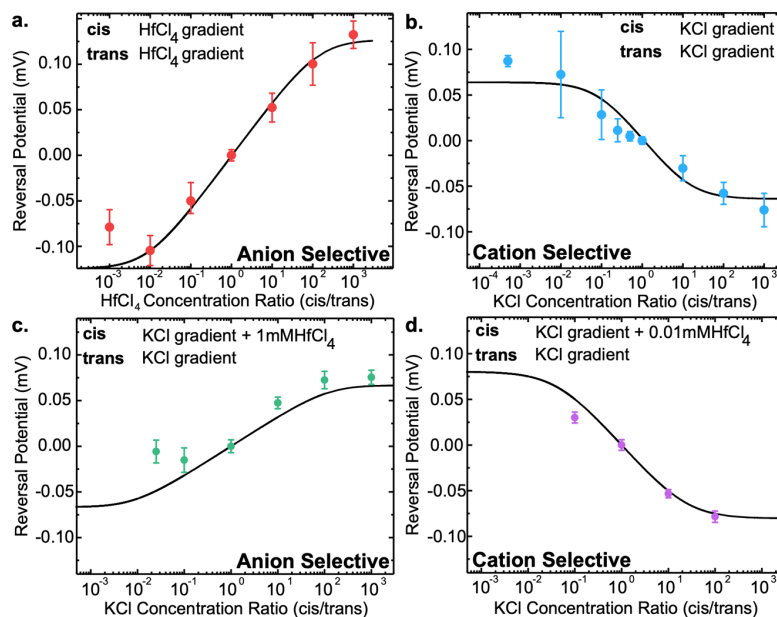
Figure 3. Selectivity ratio according to the GHK equation. Data from different cis concentration systems are combined, and an overall GHK fit is shown with the selectivity ratio as the fitting parameter and with experimental error shown as error bars. Legends indicate the salt in cis and trans (a) $HfCl_4$ is shown to be ~400 times more selective to anions over cations. (b) With KCl, the membrane is cation-selective with a ratio of 12. (c) With the addition of 1 mM $HfCl_4$ to KCl, the membrane is anion-selective with a ratio of ~500 times more selective toward anions. (d) An addition of less $HfCl_4$ (0.01 mM) preserved the cation selectivity seen with KCl, with a selective ratio toward cations of ~22.

$$V_{rev} = \frac{RT}{F} \ln\left(\frac{P_{cat/an} + \frac{C_{trans}}{C_{cis}}}{P_{cat/an} - \frac{C_{trans}}{C_{cis}} + 1} \right) \tag{2}$$

where R and F are the molar gas and Faraday constants, respectively, T is the temperature, C is the concentration, and $P_{cat/an}$ is the selectivity ratio of cations relative to that of anions. To apply this model to multivalent ions, an expanded form of the equation is used. (See the SI, section S6.) Figure 3 presents combined experimental data (symbols) for systems with monovalent, multivalent, and mixtures of ions across a variety of cis/trans concentrations against the respective fit to the full GHK equation. Using nonlinear regression, the experimental values are fit to the GHK with the selectivity ratio ($P_{cat/an}$) as the only fitting parameter. This ratio is quoted either as $P_{cat/an}$ or as its reciprocal, $P_{an/cat}$, for cation- and anion-selective systems, respectively. Whereas the GHK equation is based on a number of assumptions (see the SI, section S6), the good level of agreement with our experimental data suggests that this model provides a valid description of the underlying physical processes in our experiments. Overall, the experimental data for all systems are well modeled by applying the GHK theory, which has been expanded to handle tetravalent ions. This implies that the transport observed adheres to electrodiffusion, as described by Poisson−Nernst−Planck (PNP) with the assumptions discussed in the SI, section S6.

The striking contrast in the GHK fit between $HfCl_4$ in Figure 3a and KCl in Figure 3b is immediately clear, supporting our findings of anion- and cation-selective behavior, respectively. The magnitude of the selectivity ratio also differs between the systems. With $HfCl_4$, the system exhibits a selectivity ratio of 400 toward anions, whereas this drops to 15 with KCl. The selectivity we observe for KCl is broadly consistent with other observations in literature.[8,13,33] From

Figure 2a, it can seen that by using $HfCl_4$, as opposed to KCl, the system exhibits increased selective ion flux at lower cis concentrations. This leads to an increase by an order of magnitude in ion selectivity compared with KCl, consistent with the fits shown here. The magnitude of selectivity toward K^+ ions is maintained with the addition of 0.01 mM $HfCl_4$ to a 100 mM KCl cis reservoir (Figure 3c), not significantly affecting the selectivity ratio at 22. However, increasing the concentration of $HfCl_4$ to 1 mM in Figure 3d switches the selectivity to anion-selective, despite the lack of a gradient of $HfCl_4$ across the system. Surprisingly, with the addition of the higher concentration of $HfCl_4$, the selectivity toward anions from a gradient of KCl is now an order of magnitude higher, at 500, compared with the selectivity toward cations.

Having shown that by altering extrinsic charging effects we are able to tune ion selectivity across graphene and hBN, we now address the mode of passage through the membranes. It has previously been implied that transport occurs via intrinsic defects.[8,34,35] To better assess these potential pathways, *in situ* Raman spectroscopy, HRTEM, and membrane conductance are used. These characterization methods, with the exception of membrane, are more readily applied to graphene than to other 2D materials; however, here we assume that measuring similar membrane conductance data from both materials implies similar defect distributions, as determined for graphene by other direct measures such as TEM and Raman spectroscopy. Figure 4a shows some typical Raman spectra for monolayer graphene suspended on an electrolyte solution, with different spectra coming from distinct graphene membranes on a identical electrolyte; each spectrum is an accumulation of several repeated spectra. The spectra show a prominent 2D peak at 2685 cm^{-1} and a G peak at 1597 cm^{-1}, the intensity ratio of which is ~2.1, indicative of a monolayer sample.[36] The presence of the D peak at 1347 cm^{-1} is
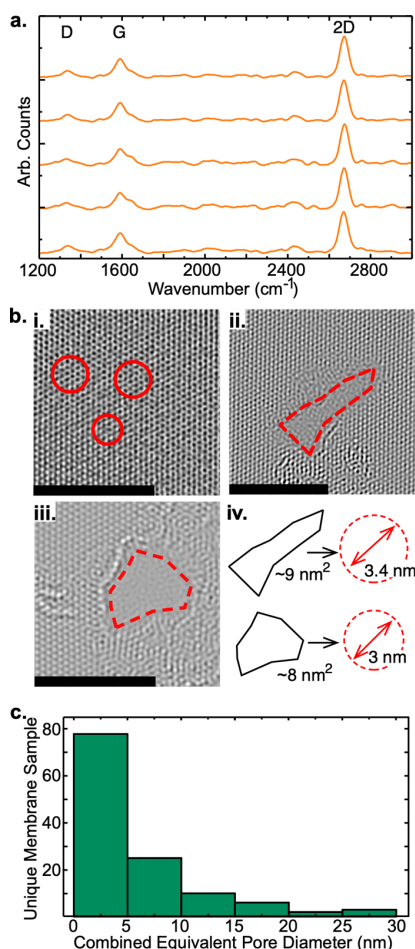
Figure 4. Membrane and pore characterization in graphene. (a) Raman spectra showing prominent 2D (2685 cm^{-1}), G (1597 cm^{-1}), and D (1347 cm^{-1}) peaks with a 2D/G intensity ratio of 2.1, which is indicative of defected monolayer graphene. Raman spectra were captured *in situ* with graphene suspended on a salt solution. Multiple spectra taken at different points for a sample of graphene floating on KCl are shown. (b) Post-exit-wave-reconstruction HRTEM phase images showing various regions of the graphene sample: (i) Stone−Wales defects are circled, (ii,iii) defected regions are shown, and (iv) defected regions are shown to have areas equivalent to a ~3 nm circular pore. Scale bar: 5 nm. (c) Distribution of the summed total circular defect area, which could account for the experimentally observed selective currents.

indicative of defects within graphene, with further characterization of graphene and hBN in the SI, section S7. Defects could take the form of large cracks or a collection of smaller scale defects referred to as edge defects. Given the nature of how the material is both fabricated and characterized, this peak is most likely attributed to a collection of smaller scale edge defects.[36] When coupled with optimized transfer and interface cleaning, CVD-grown material, as used in this Article, has been shown to have as high a mobility as "pristine" exfoliated flakes.[37] We would speculate that the most likely origin of intrinsic defects is due to standard wet-transfer methods, as used here.

Because defects within an otherwise impenetrable membrane provide the only pathway for charge to flow[38] further

characterization of the inherent defects is important. To this end, HRTEM is used on graphene samples prepared identically to those used in experiments. Some representative post-exit-wave-reconstructed images (SI, section S8) are shown in Figure 4b. Figure 4b.i shows an area of graphene where the hexagonal order of the lattice is seen alongside single atomic vacancy defects and some lattice disordering, referred to as Stone−Wales defects (red circles). These defects are, however, too small to account for selective ionic transport.[9] Figure 4b.ii,iii shows examples of larger intrinsic defects that could facilitate selective ionic transport. The area of these defects is ~8 to 9 nm^2, corresponding to an equivalent diameter of ~3 nm for a circular defect, as shown in Figure 4b.iv.

High-resolution microscopy is a powerful tool but provides only a limited view, making the extraction of large-scale statistics for the material difficult. Furthermore, it should be noted that TEM imaging is not carried out *in situ* and thus is not a direct characterization of defects through which we measure selective currents but instead is a characterization of the membrane as identically used in selectivity measurements. Therefore, for both a larger scale and a more direct quantification of such defects, an empirical approach based on the membrane conductivity is used. The conductivity is measured by taking the resistance from I−V curves for a fixed salt concentration and fixed membrane area. The contributing resistance from the capillary is subtracted (see the SI, section S9) from this to leave the conductivity of the membrane alone. Unlike TEM, this approach considers the whole membrane area and thus provides an indication of the sum total defect area across the sample. To relate the conductivity of the membrane to the density of defects, we first assume that we can approximate the conductivity through many smaller defects by that through a single larger pore with an area equal to the sum of the areas of all individual defects. For a single circular pore, the following empirical equation can be used to estimate the conductance as[39]

$$G = \sigma \left(\frac{4t}{D^2} + \frac{1}{D} \right)^{-1} \tag{3}$$

where σ is the solution conductivity, t is the membrane thickness (taken as 0.6 nm for graphene on water[39]), and D is the pore diameter. From ~130 selective membrane samples, the conductance is measured, and from this, an estimate of the size of the pore that would be required to account for the observed conductance is determined from eq 3. In Figure 4c, we plot the distribution of equivalent pore sizes for these samples. Over half of selective membrane samples show ionic flux accountable by defects of diameter 5 nm or smaller, which is consistent with the observed defects in the HRTEM images. Moreover ~75% of samples exhibit conductivities consistent with a total defect area equivalent to a 10 nm diameter circular pore or smaller. (See the SI, section S9 for a discussion of the analysis.) Having sealed onto a membrane, measurements of no appreciable conductance did not occur. Because pristine graphene is impermeable to ions and ionic conduction exclusively occurs through the sealed membrane, leakage around the rim of the capillary is negligible if present, and we assume that the observed selective flux is through these defects, although the lack of experimental *in situ* imaging means that one can only infer that these pores are the selective current pathways.

Despite much recent literature providing theoretical and experimental evidence of selectivity within pores larger than those accounted for by Debye overlap, notions that an obligatory condition for selectivity is that the Debye screening length in the system is comparable to the pore size still persist.[40−43] However, in our experiments, we observe selectivity in pores with an equivalent diameter of up to ~30 nm despite Debye lengths that can be as short as ~0.3 nm for the monovalent electrolyte and ~0.1 nm for the tetravalent electrolyte.[44] (See the SI, section S10 for Debye screening lengths in our system.) Because of how we measure conductance, the equivalent pore size could also be made up of many smaller defects; we note that based on the selectivity, we observe that these singular defects should be <3 nm.[8] If the selectivity we observe originated from larger pores, then the observations would not be fully described by Debye overlap. Because the selectivity is not limited by the size of the ion, it is also not attributable to steric effects; see the SI, section S10. However, Poggioli et al.[45] have shown that surface conductance plays a key role in generating ion selectivity, a phenomenon governed by Dukhin length overlap. It is known that the surface conductance of 2D materials is heavily affected by their substrate,[46−48] and, in keeping with this, we see Raman spectra of graphene on various concentrations of KCl/HfCl₄, which show positive/negative shifts in 2D and G peaks, indicating negative/positive surface charges, respectively; refer to the SI, section S11. A full exploration of the Dukhin length in our system would require a more careful characterization of the surface conductance, which is beyond the scope of this work. However, within this theoretical framework, selectivity has been previously demonstrated for pores measuring up to 100 nm, as reported by Rollings et al.[13] among others,[43,49] which would be consistent with our results. A key consequence of this is that the defects studied in this work could potentially be expanded (for example, by ozone treatment[3,8,14] or chemical etching[8,50]) closer to 100 nm while maintaining the selectivity. This would increase the fluid flux through the pores, increasing the selective flux and thus any potentially generated osmotic power using this system.

Finally, to assess the membrane performance for applications in power generation, in Figure 5, we show the selectivity ratios as a function of the cis reservoir concentration and a projection of the osmotic power generation for all considered systems. Here in Figure 5a, in contrast with Figure 3, the GHK-derived selectivity is extracted and shown separately for each cis reservoir concentration. (For individual analytical fits, see the SI, section S12). Given that the magnitude of selectivity is affected not just by the concentration ratio but also by the absolute value of the cis concentration, the determination of the maximum obtainable selectivity ratio, as opposed to the mean, requires systems with different cis concentrations to be considered separately. Figure 5a also shows, once again, the striking change from a cation-selective regime with KCl to an anion-selective with HfCl₄, with a clear transition point in mixed environments. The highest selectivity ratios are achieved in systems with 100 mM in the [cis] reservoir. Importantly, it is clear that the performance of hBN is comparable to that of graphene. The insulating nature of hBN, the reduced order of atomic symmetry, and the different chemical composition present it as a contrasting 2D material to graphene. Because the system with hBN responds in a way consistent with that of graphene, we can assume that the ionic transport phenomena
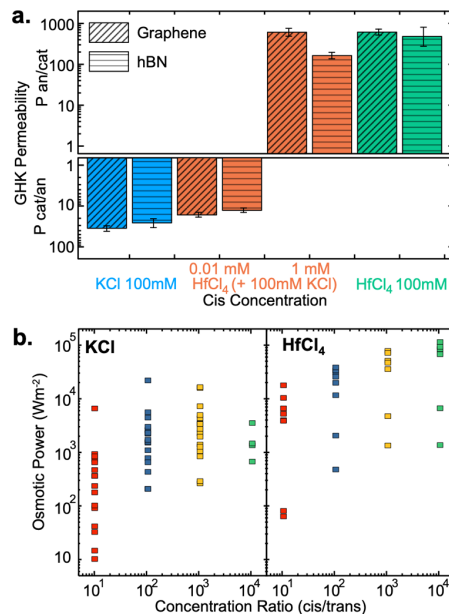

Figure 5. Selectivity ratios and power generation within our system. (a) KCl is shown as cation-selective with a higher selectivity ratio for a cis concentration of 100 mM. The addition of 0.01 mM HfCl₄ maintains cation selectivity; however, 1 mM switches to anion-selective. HfCl₄ is anion-selective with a high selectivity ratio of ~500. The behavior for both graphene and hBN is shown, showing a similar preference in both materials. (b) KCl and HfCl₄ power generation as a function of the concentration ratio using graphene are compared. HfCl₄ can generate >100 kW/m² , whereas the figure is lower at 10 kW/m² with KCl.

are extrinsic to the 2D materials themselves and are more dominated by the surface effects.

Within a would-be application such as the extraction of energy from ionic flux, Figure 5b presents the osmotic power that could be generated using our system. The osmotic power values we measure for KCl are nominally in the region of 10^3 W/m², peaking at 10^4 W/m², which agrees with previous calculations for a similar system.[8,49] Compared with KCl, the power extracted from HfCl₄ increases by 10−100 times, a significant increase, as expected from the selectivity ratios shown in Figure 5a. Reaching a peak of 10^5 W/m² potential osmotic power, this system compares favorably to the performance in enlarged graphene defects and to commercial Nafion membranes.[8] Recently, using methods of enhancing transport through pores, Graf et al.[19] estimate the extraction of 160 pW per 10 nm milled pores in MoS₂, which is on the order of 10^5 W/m² (depending on the assumed pore distribution). Our system thus provides comparable power values, and an increase seems possible if the pore size and surface charge are optimized in the future.

CONCLUSIONS

We have shown that multivalent ions can be used to alter the surface charge on 2D membranes, allowing for tunable anion/cation selectivity. By measuring the current across membranes sealed onto glass nanocapillaries in a variety of salt conditions, the magnitude and direction of selectivity have been established. Because extrinsic charge effects are known to significantly influence the selectivity across 2D membranes,

this suggests that the negative charge on the 2D membrane surface and thus around the pore is altered by multivalent ions such that the transport of anions is preferential to cations. We find that this effect can be induced in monovalent salts by the addition of a multivalent salt. The immediate implication is that the magnitude and direction of ion selectivity can be controlled and tuned extrinsically. The development of anion-selective membranes is a crucial step in furthering the understanding of surface charge interactions as well as allowing for direct application in cation/anion-selective stacked systems. Thus our finding provides potential for the use of 2D materials as ion-exchange membranes. We infer that selective transport in our system could be due to pores similar to imaged defects intrinsic to transferred CVD membranes, removing the requirement for laborious pore creation techniques. We imaged defects for as-grown graphene on the order of ~3 nm, and even for these relatively small defects, the correlated selectivity to membrane conductance shows that a high level of selective salt permeability can be achieved coupled to a lower fluid resistance. Anion selectivity is found to persist at high salt concentrations, increasing the potential osmotic power generated using these systems. Moreover, we have shown that lower conductance membranes, and thus those with enlarged defects, could remain selective and so could provide even lower fluid resistance. As such, moving forward, surface treatments allowing for the defects to be enlarged up to 100 nm, increasing the ionic flux across the membranes, would make these systems even more attractive in technological applications. Moreover, *in situ* high-resolution imagery with live selectivity experiments would directly characterize pores and correlate them with an associated selectivity, further elucidating selective current pathways in 2D membranes.

EXPERIMENTAL METHODS

Graphene Preparation. Monolayer graphene was produced in a cold-wall CVD reactor (AIXTRON BM Pro 4) using 99.8% 25 μm thick copper foil (Alfa-Aesar) as a catalyst. The copper was cleaned in acetone and isopropyl alcohol (IPA) before being partially oxidized prior to synthesis. The synthesis procedure consisted of annealing at 1070 °C in 50 mbar of argon for 30 min before being exposed to 50 mbar of a 4000:1000:1 Ar/H$_2$/CH$_4$ gas mixture for 90 min, resulting in full coverage of the copper foil by graphene (>99% monolayer, grain-size >100 μm diameter[51]), confirmed by Raman spectroscopy (Renishaw inVia) and scanning electron miscroscopy (SEM) (FEI Magellan 400), respectively; see the SI, section S7.

Hexagonal Boron Nitride Preparation. hBN material was grown similarly to the methods previously reported.[52] In brief, iron foils (100 μm, Goodfellow, 99.8%) were cleaned in acetone and IPA and loaded into a custom cold-wall CVD system with a graphite heater. The temperature was ramped to 940 °C at 50 °C/min, and the foils were annealed in an ammonia atmosphere (4 mbar, 5 min). For the hBN synthesis, borazine was added as a precursor (10^{-3} mbar, 5 min), and the system was rapidly cooled (200 °C/min initially) by turning off the heater. An electrochemical bubbling transfer method[53] was used to deposit hBN films onto SiO$_2$ substrates for Raman characterization. See the SI for further details and characterization.

Membrane Transfer. For graphene grown on copper, as described, a PMMA supporting layer was used to etch the copper using ammonium persulfate, and the subsequent PMMA–graphene layer was transferred onto cleaved KCl chips. Acetone and IPA washes were used to remove PMMA. Meanwhile, for hBN, a PMMA-free method involving an electrochemical process[53] was used to cleave onto KCl chips. Finally, gold strips were evaporated through a shadow mask onto the graphene/hBN to serve as optical guiding lines and a supporting framework.

Fluidic Cell Preparation. Quartz capillaries (Sutter) with a 0.5 mm/0.3 mm (inner/outer) diameter were sonicated in ethanol for 10 min before drying under a nitrogen stream and baking at 60 °C to remove residual ethanol. Capillaries were pulled to a nominal inner diameter of 150 nm using a laser-assisted puller (Sutter P-2000). The expected morphology and pore diameter were confirmed by SEM; see the SI for images and the pore-size distribution. Back-end of capillaries were submerged in to desired salt solution and placed in a vacuum desiccator to induce capillary filling. Filled capillaries were inserted into a holder (Axopatch Holder with Suction Port), which could be mounted to an Axopatch head stage.

Ion Selectivity Measurements. The experimental setup is shown in Figure 1a. Graphene and other 2D membranes were contacted using quartz capillaries with a 150 nm circular opening. The capillaries were first filled with a salt solution, forming the cis chamber. This was then sealed by a 2D material, forming a free-standing structure. The sealed capillary was exposed to different external salt solutions, forming the trans reservoir. Thus the material was exposed to a fixed salt in the capillary and a variable trans salt, allowing for the introduction of a salt concentration gradient across the membrane. Disposable Ag/AgCl electrodes were made by submerging pure silver wire in sodium hypochlorite for at least 1 h. Electrodes were placed on either side of the graphene membrane, one in the capillary holder (cis) and the other exposed to a salt solution (trans). To eliminate redox potentials[54] due to salinary gradients at the trans electrode, a matched agarose salt bridge was used. The electrodes were connected to the head stage of an Axopatch 200B patch clamp amplifier (Molecular Devices). All current measurements were subject to an internal amplifier Bessel filter at 10 kHz, recording at 20 kHz; each current step was recorded for 1 s with a 500 ms settling time. Preceding selectivity measurements, the amplifier voltage offset was calibrated using symmetric salt conditions. DC voltages were applied in steps of 20 mV from up to −200 to 200 mV, and the current was measured.

Data Analysis. Multiple $I-V$ curves were recorded for each data point; these were averaged, and a standard error was extracted. A linear fit was then applied to the $I-V$ measurements, extracting reversal potentials and leakage currents. A plot of the reversal potentials and leakage currents against the trans concentration was used to extract the gradient of a linear fit, exposing the measures of selectivity. Additionally, the measured reversal potentials were used to estimate ion selectivity according to the expanded GHK equation (SI, section S6) using nonlinear regression. Standard errors were used as weights in the regression, with a standard error found for the fitting parameter.

Imaging. HRTEM imaging was taken using the TEAM 0.5 microscope at Lawrence Berkeley National Laboratory. This microscope achieves high resolution through spherical aberration correction and a monochromatic beam. The microscope was operated at 80 kV to prevent knock-on damage of the graphene sample. Through-focal series images were taken from −50 to 50 nm about the focal plane. Exit wave reconstruction (see the SI, section S8) was used for the through focal series to produce HRTEM images.

ASSOCIATED CONTENT

Ⓢ Supporting Information

The Supporting Information is available free of charge at https://pubs.acs.org/doi/10.1021/acsnano.9b08168.

> Detailed example of the analysis used; derivations of GHK model equations; experimental data on divalent, trivalent, and other tetravalent ions; discussion with experimental data on pH considerations within the system; material characterization data; and further Raman spectra (PDF)

AUTHOR INFORMATION

Corresponding Author

> **Ulrich F. Keyser** — *University of Cambridge, Cambridge, United Kingdom*; Email: ufk20@cam.ac.uk

Other Authors

> **Mustafa Caglar** — *University of Cambridge, Cambridge, United Kingdom*; orcid.org/0000-0001-7547-1817

> **Inese Silkina** — *University of Cambridge, Cambridge, United Kingdom*

> **Bertram T. Brown** — *University of Cambridge, Cambridge, United Kingdom*

> **Alice L. Thorneywork** — *University of Cambridge, Cambridge, United Kingdom*

> **Oliver J. Burton** — *University of Cambridge, Cambridge, United Kingdom*

> **Vitaliy Babenko** — *University of Cambridge, Cambridge, United Kingdom*

> **Stephen Matthew Gilbert** — *University of California, Berkeley, Berkeley, California, Lawrence Berkeley National Laboratory, Berkeley, California, and Kavli Energy NanoScience Institute at the University of California, Berkeley and the Lawrence Berkeley National Laboratory, Berkeley, California*

> **Alex Zettl** — *University of California, Berkeley, Berkeley, California, Lawrence Berkeley National Laboratory, Berkeley, California, and Kavli Energy NanoScience Institute at the University of California, Berkeley and the Lawrence Berkeley National Laboratory, Berkeley, California*

> **Stephan Hofmann** — *University of Cambridge, Cambridge, United Kingdom*; orcid.org/0000-0001-6375-1459

Complete contact information is available at:
https://pubs.acs.org/10.1021/acsnano.9b08168

Notes

The authors declare no competing financial interest.

REFERENCES

(1) Varcoe, J. R.; Atanassov, P.; Dekel, D. R.; Herring, A. M.; Hickner, M. A.; Kohl, P. A.; Kucernak, A. R.; Mustain, W. E.; Nijmeijer, K.; Scott, K.; Xu, T.; Zhuang, L. Anion-Exchange Membranes in Electrochemical Energy Systems. *Energy Environ. Sci.* **2014**, *7*, 3135−3191.

(2) Ghaffour, N.; Missimer, T. M.; Amy, G. L. Technical Review and Evaluation of the Economics of Water Desalination: Current and Future Challenges for Better Water Supply Sustainability. *Desalination* **2013**, *309*, 197−207.

(3) Aliprandi, A.; Pakulski, D.; Ciesielski, A.; Samorì, P. Punctured Two-Dimensional Sheets for Harvesting Blue Energy. *ACS Nano* **2017**, *11*, 10654−10658.

(4) Luo, T.; Abdu, S.; Wessling, M. Selectivity of Ion Exchange Membranes: A Review. *J. Membr. Sci.* **2018**, *555*, 429−454.

(5) Kim, D. K.; Duan, C.; Chen, Y. F.; Majumdar, A. Power Generation from Concentration Gradient by Reverse Electrodialysis in Ion-Selective Nanochannels. *Microfluid. Nanofluid.* **2010**, *9*, 1215−1224.

(6) Sahu, S.; Zwolak, M. Colloquium: Ionic Phenomena in Nanoscale Pores through 2D Materials. *Rev. Mod. Phys.* **2019**, *91*, 21004.

(7) Hong, S.; Constans, C.; Surmani Martins, M. V.; Seow, Y. C.; Guevara Carrió, J. A.; Garaj, S. Scalable Graphene-Based Membranes for Ionic Sieving with Ultrahigh Charge Selectivity. *Nano Lett.* **2017**, *17*, 728−732.

(8) Walker, M. I.; Ubych, K.; Saraswat, V.; Chalklen, E. A.; Braeuninger-Weimer, P.; Caneva, S.; Weatherup, R. S.; Hofmann, S.; Keyser, U. F. Extrinsic Cation Selectivity of 2D Membranes. *ACS Nano* **2017**, *11*, 1340−1346.

(9) Cohen-Tanugi, D.; Grossman, J. C. Water Desalination across Nanoporous Graphene. *Nano Lett.* **2012**, *12*, 3602−3608.

(10) Kang, Y.; Zhang, Z.; Shi, H.; Zhang, J.; Liang, L.; Wang, Q.; Ågren, H.; Tu, Y. Na+ and K+ Ion Selectivity by Size-Controlled Biomimetic Graphene Nanopores. *Nanoscale* **2014**, *6*, 10666−10672.

(11) Mogg, L.; Zhang, S.; Hao, G.-P.; Gopinadhan, K.; Barry, D.; Liu, B. L.; Cheng, H. M.; Geim, A. K.; Lozada-Hidalgo, M. Perfect Proton Selectivity in Ion Transport through Two-Dimensional Crystals. *Nat. Commun.* **2019**, *10*, 4243.

(12) Bunch, J. S.; Verbridge, S. S.; Alden, J. S.; van der Zande, A. M.; Parpia, J. M.; Craighead, H. G.; McEuen, P. L. Impermeable Atomic Membranes from Graphene Sheets. *Nano Lett.* **2008**, *8*, 2458−2462.

(13) Rollings, R. C.; Kuan, A. T.; Golovchenko, J. A. Ion Selectivity of Graphene Nanopores. *Nat. Commun.* **2016**, *7*, 11408.

(14) O'Hern, S. C.; Boutilier, M. S. H.; Idrobo, J. C.; Song, Y.; Kong, J.; Laoui, T.; Atieh, M.; Karnik, R. Selective Ionic Transport through Tunable Subnanometer Pores in Single-Layer Graphene Membranes. *Nano Lett.* **2014**, *14*, 1234−1241.

(15) Zurutuza, A.; Marinelli, C. Challenges and Opportunities in Graphene Commercialization. *Nat. Nanotechnol.* **2014**, *9*, 730−734.

(16) Lin, L.; Peng, H.; Liu, Z. Synthesis Challenges for Graphene Industry. *Nat. Mater.* **2019**, *18*, 520−524.

(17) Kobayashi, T.; Bando, M.; Kimura, N.; Shimizu, K.; Kadono, K.; Umezu, N.; Miyahara, K.; Hayazaki, S.; Nagai, S.; Mizuguchi, Y.; Murakami, Y.; Hobara, D. Production of a 100-m-Long High-Quality Graphene Transparent Conductive Film by Roll-to-Roll Chemical Vapor Deposition and Transfer Process. *Appl. Phys. Lett.* **2013**, *102*, 023112.

(18) Chin, H. T.; Lee, J. J.; Hofmann, M.; Hsieh, Y. P. Impact of Growth Rate on Graphene Lattice-Defect Formation within a Single Crystalline Domain. *Sci. Rep.* **2018**, *8*, 3−8.

(19) Graf, M.; Lihter, M.; Unuchek, D.; Sarathy, A.; Leburton, J.-P.; Kis, A.; Radenovic, A. Light-Enhanced Blue Energy Generation Using MoS$_2$ Nanopores. *Joule* **2019**, *3*, 1549−1564.

(20) Koenig, S. P.; Wang, L.; Pellegrino, J.; Bunch, J. S. Selective Molecular Sieving through Porous Graphene. *Nat. Nanotechnol.* **2012**, *7*, 728−32.

(21) Rabchinskii, M. K.; Shnitov, V. V.; Dideikin, A. T.; Aleksenskii, A. E.; Vul', S. P.; Baidakova, M. V.; Pronin, I. I.; Kirilenko, D. A.; Brunkov, P. N.; Weise, J.; Molodtsov, S. L. Nanoscale Perforation of Graphene Oxide during Photoreduction Process in the Argon Atmosphere. *J. Phys. Chem. C* **2016**, *120*, 28261−28269.

(22) Walker, M. I.; Weatherup, R. S.; Bell, N. A. W.; Hofmann, S.; Keyser, U. F. Free-Standing Graphene Membranes on Glass Nanopores for Ionic Current Measurements. *Appl. Phys. Lett.* **2015**, *106*, 023119.

(23) Besteman, K.; Zevenbergen, M. A. G.; Lemay, S. G. Charge Inversion by Multivalent Ions: Dependence on Dielectric Constant and Surface-Charge Density. *Phys. Rev. E* **2005**, *72*, 1−9.

(24) van der Heyden, F. H. J.; Stein, D.; Besteman, K.; Lemay, S. G.; Dekker, C. Charge Inversion at High Ionic Strength Studied by Streaming Currents. *Phys. Rev. Lett.* **2006**, *96*, 1−4.

(25) Besteman, K.; Zevenbergen, M. A. G.; Heering, H. A.; Lemay, S. G. Direct Observation of Charge Inversion by Multivalent Ions as a Universal Electrostatic Phenomenon. *Phys. Rev. Lett.* **2004**, *93*, 4−7.

(26) Hille, B. *Ionic Channels of Excitable Membranes*; Sinauer Associates: Sunderland, MA, 2001; pp 450−460.

(27) Weber, M.; Koonkaew, B.; Balme, S.; Utke, I.; Picaud, F.; Iatsunskyi, I.; Coy, E.; Miele, P.; Bechelany, M. Boron Nitride Nanoporous Membranes with High Surface Charge by Atomic Layer Deposition. *ACS Appl. Mater. Interfaces* **2017**, *9*, 16669−16678.

(28) Grosjean, B.; Bocquet, M. L.; Vuilleumier, R. Versatile Electrification of Two-Dimensional Nanomaterials in Water. *Nat. Commun.* **2019**, *10*, 1−8.

(29) Sint, K.; Wang, B.; Král, P. Selective Ion Passage through Functionalized Graphene Nanopores. *J. Am. Chem. Soc.* **2008**, *130*, 16448−16449.

(30) He, Z.; Zhou, J.; Lu, X.; Corry, B. Bioinspired Graphene Nanopores with Voltage-Tunable Ion Selectivity for Na$^+$ and K$^+$. *ACS Nano* **2013**, *7*, 10148−10157.

(31) Zhao, Y.; Shi, W.; Van der Bruggen, B.; Gao, C.; Shen, J. Tunable Nanoscale Interlayer of Graphene with Symmetrical Polyelectrolyte Multilayer Architecture for Lithium Extraction. *Adv. Mater. Interfaces* **2018**, *5*, 1701449.

(32) Sun, P.; Zheng, F.; Zhu, M.; Song, Z.; Wang, K.; Zhong, M.; Wu, D.; Little, R. B.; Xu, Z.; Zhu, H. Selective Trans-Membrane Transport of Alkali and Alkaline Earth Cations through Graphene Oxide Membranes Based on Cation-π Interactions. *ACS Nano* **2014**, *8*, 850−859.

(33) Cantley, L.; Swett, J. L.; Lloyd, D.; Cullen, D. A.; Zhou, K.; Bedworth, P. V.; Heise, S.; Rondinone, A. J.; Xu, Z.; Sinton, S.; Bunch, J. S. Voltage Gated Inter-Cation Selective Ion Channels from Graphene Nanopores. *Nanoscale* **2019**, *11*, 9856−9861.

(34) O'Hern, S. C.; Stewart, C. A.; Boutilier, M. S.; Idrobo, J. C.; Bhaviripudi, S.; Das, S. K.; Kong, J.; Laoui, T.; Atieh, M.; Karnik, R. Selective Molecular Transport through Intrinsic Defects in a Single Layer of CVD Graphene. *ACS Nano* **2012**, *6*, 10130−10138.

(35) Jain, T.; Rasera, B. C.; Guerrero, R. J. S.; Boutilier, M. S.; O'Hern, S. C.; Idrobo, J. C.; Karnik, R. Heterogeneous Sub-Continuum Ionic Transport in Statistically Isolated Graphene Nanopores. *Nat. Nanotechnol.* **2015**, *10*, 1053−1057.

(36) Ferrari, A. C.; Meyer, J. C.; Scardaci, V.; Casiraghi, C.; Lazzeri, M.; Mauri, F.; Piscanec, S.; Jiang, D.; Novoselov, K. S.; Roth, S.; Geim, A. K. Raman Spectrum of Graphene and Graphene Layers. *Phys. Rev. Lett.* **2006**, *97*, No. 187401.

(37) De Fazio, D.; Purdie, D. G.; Ott, A. K.; Braeuninger-Weimer, P.; Khodkov, T.; Goossens, S.; Taniguchi, T.; Watanabe, K.; Livreri, P.; Koppens, F. H.; Hofmann, S.; Goykhman, I.; Ferrari, A. C.; Lombardo, A. High-Mobility, Wet-Transferred Graphene Grown by Chemical Vapor Deposition. *ACS Nano* **2019**, *13*, 8926−8935.

(38) Celebi, K.; Buchheim, J.; Wyss, R. M.; Droudian, A.; Gasser, P.; Shorubalko, I.; Kye, J.-I.; Lee, C.; Park, H. G. Ultimate Permeation across Atomically Thin Porous Graphene. *Science* **2014**, *344*, 289−292.

(39) Garaj, S.; Hubbard, W.; Reina, A.; Kong, J.; Branton, D.; Golovchenko, J. A. Graphene as a Subnanometre Trans-Electrode Membrane. *Nature* **2010**, *467*, 190−193.

(40) Plecis, A.; Schoch, R. B.; Renaud, P. Ionic Transport Phenomena in Nanofluidics: Experimental and Theoretical Study of the Exclusion-Enrichment Effect on a Chip. *Nano Lett.* **2005**, *5*, 1147−1155.

(41) Schoch, R. B.; Han, J.; Renaud, P. Transport Phenomena in Nanofluidics. *Rev. Mod. Phys.* **2008**, *80*, 839−883.

(42) Ghosh, M.; Jorissen, K. F. A.; Wood, J. A.; Lammertink, R. G. H. Ion Transport through Perforated Graphene. *J. Phys. Chem. Lett.* **2018**, *9*, 6339−6344.

(43) Feng, J.; Graf, M.; Liu, K.; Ovchinnikov, D.; Dumcenco, D.; Heiranian, M.; Nandigana, V.; Aluru, N. R.; Kis, A.; Radenovic, A. Single-Layer MoS$_2$ Nanopores as Nanopower Generators. *Nature* **2016**, *536*, 197−200.

(44) McBride, A.; Kohonen, M.; Attard, P. The Screening Length of Charge-Asymmetric Electrolytes: A Hypernetted Chain Calculation. *J. Chem. Phys.* **1998**, *109*, 2423−2428.

(45) Poggioli, A. R.; Siria, A.; Bocquet, L. Beyond the Tradeoff: Dynamic Selectivity in Ionic Transport and Current Rectification. *J. Phys. Chem. B* **2019**, *123*, 1171−1185.

(46) Decker, R.; Wang, Y.; Brar, V. W.; Regan, W.; Tsai, H. Z.; Wu, Q.; Gannett, W.; Zettl, A.; Crommie, M. F. Local Electronic Properties of Graphene on a BN Substrate *via* Scanning Tunnelling Microscopy. *Nano Lett.* **2011**, *11*, 2291−2295.

(47) Zhu, Y.; Murali, S.; Cai, W.; Li, X.; Suk, J. W.; Potts, J. R.; Ruoff, R. S. Graphene and Graphene Oxide: Synthesis, Properties, and Applications. *Adv. Mater.* **2010**, *22*, 3906−3924.

(48) Gao, M.; Pan, Y.; Zhang, C.; Hu, H.; Yang, R.; Lu, H.; Cai, J.; Du, S.; Liu, F.; Gao, H. J. Tunable Interfacial Properties of Epitaxial Graphene on Metal Substrates. *Appl. Phys. Lett.* **2010**, *96*, 053109.

(49) Purcell, S. T.; Bocquet, L.; Siria, A.; Biance, A.-L.; Poncharal, P.; Fulcrand, R.; Blase, X. Giant Osmotic Energy Conversion Measured in a Single Transmembrane Boron Nitride Nanotube. *Nature* **2013**, *494*, 455−458.

(50) Dash, S.; Patel, S.; Mishra, B. K. Oxidation by Permanganate: Synthetic and Mechanistic Aspects. *Tetrahedron* **2009**, *65*, 707−739.

(51) Burton, O. J.; Babenko, V.; Veigang-Radulescu, V. P.; Brennan, B.; Pollard, A. J.; Hofmann, S. The Role and Control of Residual Bulk Oxygen in the Catalytic Growth of 2D Materials. *J. Phys. Chem. C* **2019**, *123*, 16257−16267.

(52) Caneva, S.; Weatherup, R. S.; Bayer, B. C.; Blume, R.; Cabrero-Vilatela, A.; Braeuninger-Weimer, P.; Martin, M. B.; Wang, R.; Baehtz, C.; Schloegl, R.; Meyer, J. C.; Hofmann, S. Controlling Catalyst Bulk Reservoir Effects for Monolayer Hexagonal Boron Nitride CVD. *Nano Lett.* **2016**, *16*, 1250−1261.

(53) Gao, L.; Ren, W.; Xu, H.; Jin, L.; Wang, Z.; Ma, T.; Ma, L. P.; Zhang, Z.; Fu, Q.; Peng, L. M.; Bao, X.; Cheng, H. M. Repeated Growth and Bubbling Transfer of Graphene with Millimetre-Size Single-Crystal Grains Using Platinum. *Nat. Commun.* **2012**, *3*, 697−699.

(54) Shao, X. M.; Feldman, J. L. Micro-Agar Salt Bridge in Patch-Clamp Electrode Holder Stabilizes Electrode Potentials. *J. Neurosci. Methods* **2007**, *159*, 108−115.